RSC Advances

PAPER

View Article Online
View Journal | View Issue

Cite this: *RSC Adv.*, 2022, **12**, 20838

Colorimetric assay based on $NiCo_2S_4$@N,S-rGO nanozyme for sensitive detection of H_2O_2 and glucose in serum and urine samples†

Hanzhang Ye,‡ Yongli Ding,‡ Tingting Liu, Jiani Li, Qi Wang, Yuhao Li, Jingjing Gu, Zhanen Zhang * and Xuedong Wang *

Traditional bimetallic sulfide-based nanomaterials often have a small specific surface area (SSA), low dispersion, and poor conductivity, thereby limiting their wide applications in the nanozyme-catalytic field. To address the above issues, we herein integrated $NiCo_2S_4$ with N,S-rGO to fabricate a nanocomposite ($NiCo_2S_4$@N,S-rGO), which showed a stronger peroxidase–mimetic activity than its pristine components. The SSA (155.8 $m^2\ g^{-1}$) of $NiCo_2S_4$@N,S-rGO increased by ~2-fold compared to $NiCo_2S_4$ with a pore size of 7–9 nm, thus providing more active sites and charge transfer channels. Based on the Michaelis–Menten equation, the affinity of this nanocomposite increased 40% and 1.1~10.6-fold compared with $NiCo_2S_4$ with N,S-rGO, respectively, highlighting the significant enhancement of the peroxidase-like activity. The enhanced activity of this nanocomposite is derived from the joint participation of $^{\bullet}OH$, $^{\bullet}O_2^-$, and photogenerated holes (h^+), and was dominated by h^+. To sum up, N,S-codoping, rich S-vacancies, and multi-valence states for this nanocomposite facilitate electron transfer and accelerate reaction processes. The nanocomposite-based colorimetric sensor gave low detection limits for H_2O_2 (12 μM) and glucose (0.3 μM). In comparison with the results detected by a common glucose meter, this sensor provided the relative recoveries across the range of 97.4–101.8%, demonstrating its high accuracy. Moreover, it exhibited excellent selectivity for glucose assay with little interference from common co-existing macromolecules/ions, as well as high reusability (>6 times). Collectively, the newly developed colorimetric sensor yields a promising methodology for practical applications in H_2O_2 and glucose detection with advantages of highly visual resolution, simple operation, convenient use, and satisfactory sensitivity.

Received 3rd June 2022
Accepted 7th July 2022

DOI: 10.1039/d2ra03444a

rsc.li/rsc-advances

1 Introduction

Diabetes is a chronic disease caused by insulin secretion defects or insulin dysfunction. Severe diabetes can lead to various acute and chronic complications, such as cardiovascular disease, diabetic ketoacidosis, renal dysfunction, insomnia, and so on.[1,2] The International Diabetes Federation (IDF) projects that nearly 592 million people worldwide will have diabetes by 2035.[3] Timely monitoring of patients' blood glucose and urine sugar level plays an extremely important role in the prevention and control of diabetes. Hydrogen peroxide (H_2O_2) acts as one of the important signaling molecules regulating fundamental biological processes, while an escalated level of H_2O_2 can trigger irreversible oxidative damage of lipids, proteins and DNA, as well as some diseases such as neurodegeneration, diabetes, Alzheimer's disease, and even cancer.[4] Thus, it is of practical significance to develop a rapid, sensitive, efficient and inexpensive H_2O_2 and glucose assay methodology.

At present, a variety of approaches for the detection of glucose and H_2O_2 have been established, such as enzymatic methods,[5] glucose meters,[6] electrochemical non-enzymatic methods,[7–11] high performance liquid chromatography (HPLC),[12] capillary zone electrophoresis,[13] Fourier transform infrared spectroscopy (FT-IR),[14] *etc.* The aforementioned methods have many kinds of drawbacks, such as difficult storage of natural enzymes, complex pretreatment procedures prior to chromatographic, spectrometric, and electrochemical detection, low sensitivity of glucose meter, *etc.*[15,16] Relatively, colorimetric approaches based on horseradish peroxidase (HRP) have attracted much attention because of their simplicity, rapidity, small background interference, and high sensitivity.[17] However, HRP, an important natural enzyme, is costly to prepare and not easily stored after denaturation, heating or chemical changes. In recent years, novel nanozymes with peroxidase-like activity have been developed as alternatives to address the above issues of natural enzymes, such as high cost, difficult storage, *etc.* It is worth noting that their

Jiangsu Key Laboratory of Environmental Science and Engineering, School of Environmental Science and Engineering, Suzhou University of Science and Technology, Suzhou 215009, China. E-mail: zjuwxd@163.com; zhangzhanen@126.com

† Electronic supplementary information (ESI) available. See https://doi.org/10.1039/d2ra03444a

‡ These authors contributed equally to this work.

applications in the detection of glucose and H_2O_2 have become a research hotspot.[18,19]

Since the first introduction of Fe_3O_4 with peroxidase-like activity,[20] various nanomaterials have been widely developed as various colorimetric sensing platforms, including metal oxides,[21] biological carbon-based materials,[22] metal organic frameworks with porous structure,[23] and various nanohybrids and their derivatives.[24] Zhou's team (2022) prepared Cu/N co-doped carbon-based nanozyme (Cu/NC NS) by pyrolysis by utilizing two-dimensional Cu nanosheet as metal precursor, g-C_3N_4 as nitrogen source and carbon substance, which possessed superior peroxidase-like activity of copper based nanomaterials.[25] Liu's teamwork (2019) synthesized a novel nanozyme by decorating highly dispersed ultrafine IrO_2 nanoparticles on reduced graphene oxide (rGO) nanosheets, and found that the IrO_2@rGO exhibited intrinsic peroxidase-like activity to catalyze 3,3′,5,5′-tetramethylbenzidine (TMB) oxidation to produce a blue color in the presence of H_2O_2.[26] He and coworkers (2021) prepared porphyrin functionalized urchin-like $CuCo_2O_4$ nanospheres and successfully developed a colorimetric sensor for dopamine detection in human serum based on the inhibitory effect on TMBox.[27] By virtue of the synergistic-enhancing oxidase activity between 2D Co_3O_4 substrate and Rh nano particles, the obtained 2D Co_3O_4@Rh catalyzed the oxidation of TMB to blue TMBox with superior oxidase-like performance for visual sensing of bioactive urea and *p*-aminopenol.[28] A metal–organic framework-derived $NiCo_2O_4$ was confirmed to have both peroxidase-like and oxidase-like activities, which could oxidize colorless TMB to blue TMBox in the absence of H_2O_2.[29]

Compared to the corresponding metal compounds or metal oxides, the transition metal sulfides have better redox properties and are considered as promising nanoenzymes.[30] Borthakur *et al.* (2021) fabricated transition metal sulfide/porous rGO-based nanohybrids with intrinsic peroxidase-like activity, and developed a simple colorimetric sensor utilizing the feature that Hg(II) inhibited nanozymes.[31] The bimetallic sulfide, especially for $NiCo_2S_4$, is feasible for constructing a colorimetric sensing platform based on its high peroxidase activity from complex crystal structure and polyvalent state.[32] However, the small specific surface area (SSA) and poor electrical conductivity affect the catalytic activity and stability of $NiCo_2S_4$. Comparatively, owing to high SSA and stability, rGO is often employed to improve the conductivity and structural stability of $NiCo_2S_4$ and to increase the active sites and catalytic efficiency.[33,34] Liu and coworkers (2022) synthesized α-Fe_2O_3@rGO to increase the electron transfer ability, prevented the agglomeration of Fe_2O_3 and enhanced its photo Fenton catalytic ability.[35] Interestingly, the introduction of heteroatoms such as N, S, and B can also improve the catalytic activity of nanoenzymes. Due to the doping of heteroatoms, the structures of the pristine nanomaterials form a certain degree of lattice distortion, resulting in more defects and changes in electronic structures of the doped atoms near heteroatoms, and thus the catalytic activities of the doped nanomaterials are greatly improved.

Lighted by the previous research findings, this study aims to construct a highly efficient nanozyme by employing the advantages of the doping of heteroatoms, bimetallic sulfide, as well as high SSA and strong dispersion of rGO. As a proof-of-concept, we anchored $NiCo_2S_4$ onto the N,S-doped rGO to design a nanocomposite of $NiCo_2S_4$@N,S-rGO by a facile hydrothermal method. The as-constructed nanocomposite was confirmed to have higher SSA, stability, and superior peroxidase–mimetic activity than its pristine component $NiCo_2S_4$. The catalytic behavior of $NiCo_2S_4$@N,S-rGO conformed to the Michaelis–Menten equation, which could oxidize colorless TMB to blue TMBox in the presence of H_2O_2. A series of important variables were optimized to acquire the highly efficient chromogenesis. Under optimized conditions, a visual detection platform based on the as-constructed nanozyme was developed for sensitive detection of H_2O_2 and glucose in human urine and serum samples.

2 Experimental section

2.1 Chemicals and reagents

The following chemicals and regents were purchased from Aladdin (Shanghai, China): $CoCl_2 \cdot 6H_2O$, $Ni(CH_3COO)_2 \cdot 4H_2O$, thioacetamide (TAA), *p*-benzoquinone (PBQ), isopropanol (IPA), disodium ethylenediamine tetraacetate (EDTA-2Na), ethylene glycol (EG), acetic acid (HAC), dimethyl sulfoxide (DMSO), sodium acetate (NaAc), and TMB. GO was achieved from Xianfeng Nanomaterial Technology Corporation (Nanjing, China). Ultrapure water (>18.2 MΩ) was generated with a Milli-Q Gradient system (Bedford, MA, USA). All reagents were used when received without further purification.

2.2 Instruments for synthesis and characterization

The following instruments were used to synthesize the $NiCo_2S_4$,-N,S-rGO, and $NiCo_2S_4$@N,S-rGO: KQ-500DE numerical control ultrasonic cleaner (Kunshan Ultrasonic Instrument Corporation, Kunshan, China), OTF-1200× tubular furnace (Hefei Kejing Material Technology, Hefei, China), DHG-9070a electric blast drying oven (Xiwen Biotechnology, Shanghai, China), B15-3 multifunctional constant temperature and speed magnetic stirrer (Shanghai Sile Instrument Corporation, Shanghai, China), and PB-10 pH meter (Sedolis Scientific Instrument, Nanjing, China).

Transmission electron microscopy (TEM) images of the $NiCo_2S_4$, N,S-rGO, and $NiCo_2S_4$@N,S-rGO were recorded on a Talos F200S (Thermo Scientific, USA), which was operated at an accelerating voltage of 200 kV. X-ray photoelectron spectroscopy (XPS) measurement was conducted on an ESCALAB 250Xi with Al K_α source (Thermo Scientific, USA). Fourier transform infrared (FT-IR) spectra were determined on a Bruker Tensor II spectrometer (Berlin, Germany). All ultraviolet-visible absorbance was measured on a UV-2600 spectrophotometer (Shimadzu Company, Tokyo, Japan).

2.3 Preparation of the $NiCo_2S_4$, N, S-rGO, and $NiCo_2S_4$@N, S-rGO

To prepare the $NiCo_2S_4$@N,S-rGO nanocomposite, 31.1 mg of $Ni(CH_3COO)_2 \cdot 4H_2O$, 59.48 mg of $CoCl_2 \cdot 6H_2O$, and 187.82 mg of TAA were dissolved in 5 mL of ethylene glycol and stirred at ambient conditions for 30 min at 500 rpm to achieve a homogeneous solution A. Subsequently, 10 mg of GO was

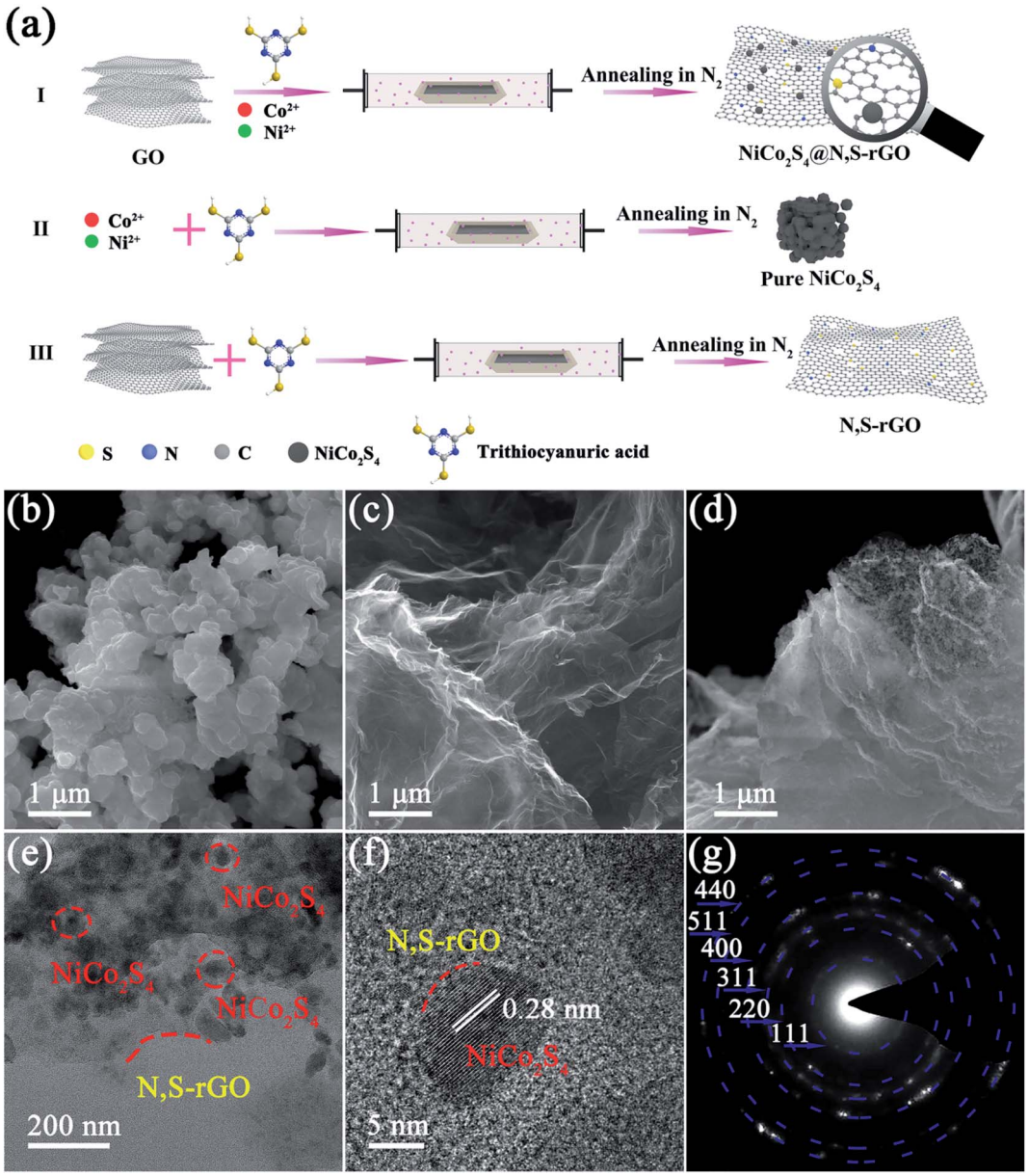

Fig. 1 (a) Schematic diagram of the overall fabrication procedures for the $NiCo_2S_4$@N,S-rGO. (b) SEM image of the $NiCo_2S_4$. (c) SEM image of the N,S-rGO. (d) SEM image of the $NiCo_2S_4$@N,S-rGO. (e) TEM image of the $NiCo_2S_4$@N,S-rGO. (f) HRTEM image of the $NiCo_2S_4$@N,S-rGO. (g) Selected area electron diffraction (SAED) of the $NiCo_2S_4$@N,S-rGO.

added to 2 mL of ethylene glycol and sonicated for 30 min to make it well dispersed, and the resultant solution was dropwise added to the aforementioned solution A under ultrasonic conditions. The final mixed solution was calcined at 300 °C under N_2 atmosphere with a heating rate of 5 °C min^{-1} for 60 min. The calcined material was washed with deionized water and ethanol alternately three times, and oven-dried at 60 °C. The final dark gray material was $NiCo_2S_4$@N,S-rGO (Fig. 1a(I)).

By way of contrast, $NiCo_2S_4$ was acquired in the absence of GO in the synthetic procedures (Fig. 1a(II)), and N,S-rGO was obtained without adding cobalt and nickel salts in the preparation processes (Fig. 1a(III)).

2.4 Peroxidase-like activity of the $NiCo_2S_4$@N,S-rGO

The catalytic reaction of TMB (a typical chromogenic substrate) was used to evaluate the peroxidase-like activity of $NiCo_2S_4$@N,S-rGO. In brief, 60 μL of $NiCo_2S_4$@N,S-rGO (1 mg mL^{-1}), 200 μL of TMB (6 mM) and H_2O_2 (50 mM) were incubated at 40 °C for 20 min in 2 mL of NaAc-HAc buffer solution (pH 4.0). The 652 nm absorbance of reaction solution was recorded on a UV-2600 spectrophotometer.

2.5 Sample preparation

Human serum and urine samples were gratis supplied by the First Affiliated Hospital of Wenzhou Medical University (Wenzhou, China). The samples were stored at 4 °C for

subsequent use within 15 days. Prior to use, the pretreated serum samples were diluted by 100-fold for H_2O_2 and glucose assay.

2.6 Ethics statement

All experiments were performed in accordance with the guidelines of the Institutional Animal Care and Use Committee. Experiments were approved by the ethics committee at Suzhou University of Science and Technology, as well as Wenzhou Medical University. Informed consents were obtained from human participants of this study.

2.7 H_2O_2 and glucose assay

As for H_2O_2 assay, 60 μL of 1 mg L^{-1} $NiCo_2S_4$@N,S-rGO suspension was added to 1700 μL NaAc-HAC buffer solution (20 mM, pH 4.0), which was referred to solution B. Subsequently, 200 μL of 6 mM TMB (dissolved with DMSO) and 40 μL of H_2O_2 solution at varying concentrations were added to solution B and mixed ultrasonically. The mixed solution was incubated at 40 °C for 20 min, and the resulting blue solution was filtered with 0.45 μm nylon member filter, diluted with Milli-Q ultrapure water and subjected to UV-vis spectral analysis at 652 nm.

The procedures for detecting glucose were similar to H_2O_2 assay, except for that the different concentrations of H_2O_2 solutions were replaced by the glucose solutions after incubation with glucose oxidase (GO_x) at 40 °C for 30 min. Under the optimized experimental conditions, the cyclability of the prepared nano-enzyme was studied. $NiCo_2S_4$@N,S-rGO washed with ethanol and water, centrifuged and filtered for collection.

3 Results and discussion

3.1 Characterization of $NiCo_2S_4$@N,S-rGO and its precursors

The overall preparation process of $NiCo_2S_4$@N,S-rGO is vividly elaborated in Fig. 1a. Briefly, the mixed solution of $CoCl_2$, $Ni(OCOCH_3)_2$ and TAA was dripped into the suspension of GO, and the Ni^{2+} and Co^{2+} were well dispersed and integrated with GO due to the electrostatic adsorption (Fig. 1a(I)). Under N_2 atmosphere, C═S, C–N, and –NH_2 in TAA provided N and S sources for the as-fabricated nanocomposite, and an excessive S source was conducive to the formation of vacant sites onto the nanosheets. The $NiCo_2S_4$, N,S-rGO, and $NiCo_2S_4$@N,S-rGO were morphologically characterized by SEM and TEM. Owing to the absence of GO, the $NiCo_2S_4$ showed agglomerates, which were composed of irregular particles (Fig. 1b). As exhibited in Fig. 1c, N,S-rGO nanosheets contained abundant folds. For the $NiCo_2S_4$@N,S-rGO, a large number of small particles were distributed on the surface of N,S-rGO nanosheets, thereby avoiding agglomeration of $NiCo_2S_4$ and providing more reactive sites. Moreover, the TEM and HRTEM images of $NiCo_2S_4$@N,S-rGO demonstrated the homogeneous dispersion of $NiCo_2S_4$ nanoparticles on the N,S-codoped graphene sheets (Fig. 1e and f). More interestingly, the HRTEM image showed that the N,S-rGO nanosheets were well integrated with the $NiCo_2S_4$ particles to form the uniform composite structure with the lattice fringes of ~0.28 nm, which accorded well with the (311) plane of $NiCo_2S_4$ (Fig. 1f). The clear boundary between $NiCo_2S_4$ and N,S-rGO proved that the Ni and S atoms were well dispersed on the surface of N,S-rGO. The corresponding selected area electron diffraction (SAED) patterns displayed the polycrystallinity of $NiCo_2S_4$, which was associated with the bright circular rings of the (111), (220), (311), (400), (511), and (440) planes of $NiCo_2S_4$. Furthermore, EDS elemental mapping (Fig. S2.†) demonstrated the presence of Ni, Co, S, C, N, evidencing the formation of $NiCo_2S_4$@N,S-rGO.

By XRD analysis, we observed very clear diffraction peaks for both $NiCo_2S_4$ and $NiCo_2S_4$@N,S-rGO (Fig. 2a). The diffraction peaks (2θ) at 16.34°, 26.83°, 31.59°, 38.32°, 47.41°, 50.46°, and 55.33° were in good agreement with the crystals (111), (220), (311), (400), (511), and (440) of the hexagonal phase of $NiCo_2S_4$ (JCPDS#20-0782), which was consistent with what has been reported previously.[36,37] These XRD data provide strong evidence that the as-fabricated nanocomposite did not change structure of the pristine nanomaterial, which was in keeping with our SAED test results.

Through Raman spectral analyses (500–2000 cm^{-1}), two peaks were found at 1350 cm^{-1} and 1590 cm^{-1} (Fig. 2b), corresponding to the characteristic Raman modes of carbon in D-

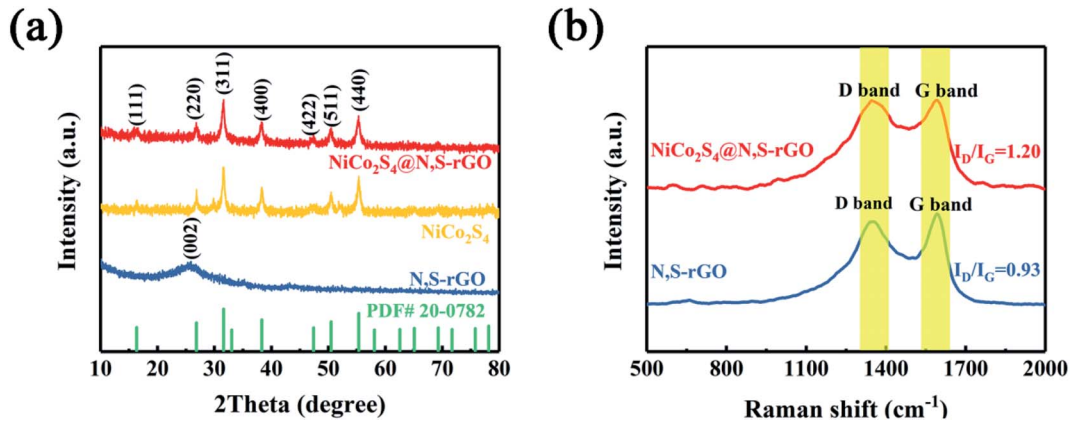

Fig. 2 (a) XRD patterns of the $NiCo_2S_4$@N,S-rGO, $NiCo_2S_4$ and N,S-rGO. (b) Raman spectra of the $NiCo_2S_4$@N,S-rGO, and N,S-rGO.

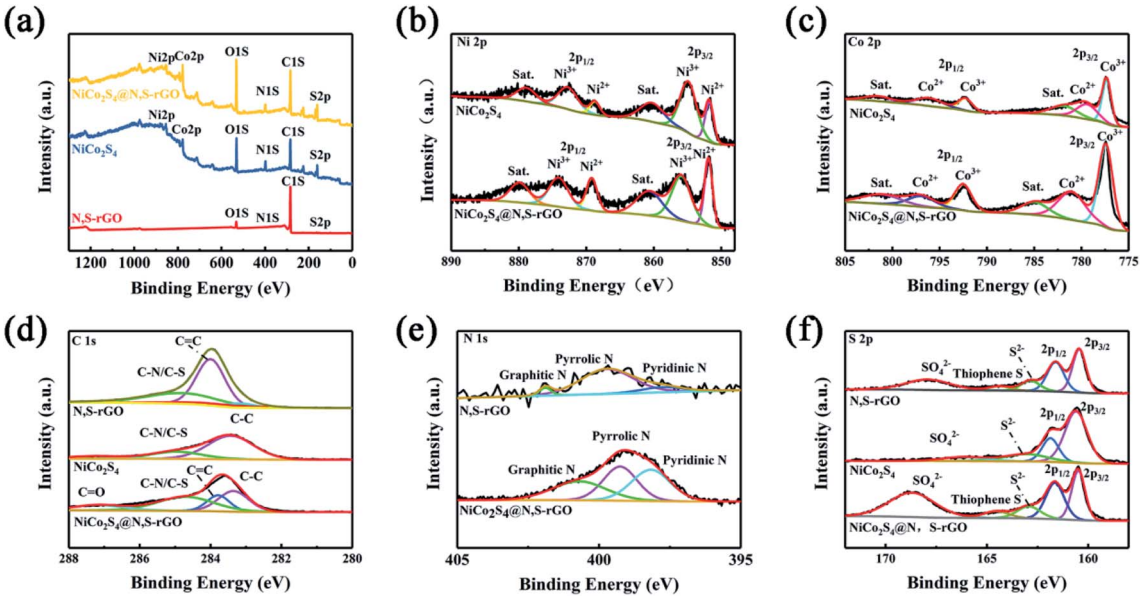

Fig. 3 (a) XPS spectra of the $NiCo_2S_4$@N,S-rGO, $NiCo_2S_4$ and N,S-rGO; (b) Ni 2p; (c) Co 2p; (d) C 1s; (e) N 1s; and (f) S 2p.

band (disordered carbon) and G-band (ordered graphite carbon), respectively. The G-band, the main characteristic peak of graphene, is caused by the in-plane vibration of sp^2 hybrid carbon atoms. D-band is generally regarded as the disordered vibration peak of graphene and is used to characterize structural defects or edges in graphene samples.[38] Compared to N, S-rGO, the $NiCo_2S_4$@N,S-rGO composite had a higher I_D/I_G ratio, implying that graphene in the composite had more defect sites, which might strongly affect the electron transfer characteristics. By IR spectra (Fig. S1†), the presence of many kinds of oxygenated functional groups (C=O, C=C, and C–O) indicated the successful recombination of $NiCo_2S_4$ and N,S-rGO. It is worth mentioning that C=O, C–N, and other functional groups provide many types of active sites for the peroxidase-like activity of nanocomposite.

XPS spectroscopy was employed to characterize the composition of $NiCo_2S_4$, N,S-rGO, and $NiCo_2S_4$@N,S-rGO (Fig. 3a). Correspondingly, the peaks at 872.8 and 855.0 eV were attributed to Ni^{3+}, while the peaks at 868.7 and 851.7 eV to Ni^{2+} (Fig. 3b). In particular, the 163 eV peak corresponding to S_2^{2-} indicated the occurrence of S vacancy in the $NiCo_2S_4$@N,S-rGO. The peaks at 792.5 and 777.4 eV belonged to Co^{3+}, while those at 796.3 and 779.4 eV were ascribed to Co^{2+} (Fig. 3c). The multivalence states of complex Co and Ni were favorable for the strengthening of electrical conductivity, especially trivalent Co and Ni. The C 1s core-level spectrum showed the peaks with the binding energies of 287.3, 284.6, 283.8 ev for C=O, C–N/C–S, C=C bonding, respectively (Fig. 3d). These peaks revealed the successful doping of the N and S heteroatoms into the carbon matrix, which was in general agreement with the results of N,S-rGO. Also, the high-resolution spectra of S and N verified the efficient incorporation of heteroatoms. As for the N 1s spectra of $NiCo_2S_4$@N,S-rGO and N,S-rGO, these deconvolution peaks at 400.9, 399.3, and 398.3 eV were ascribed to graphitic N, pyrrole-type N, and pyridine-type N, respectively (Fig. 3e). With regard to the XPS spectrum of S 2p, the peaks at 161.6 and 160.4 eV corresponded to the peaks of S^{2-}, and the 164.5 eV peak for the N,S-rGO and $NiCo_2S_4$@N,S-rGO was thiophene S (Fig. 3f), indicating that S atoms were doped in the carbon-based heterocyclic structure.

Fig. S3† displays distinct EPR signals of S-vacancy with a g-factor of 2.004. In contrast to $NiCo_2S_4$, the $NiCo_2S_4$@N,S-rGO showed the higher EPR signal, suggesting an abundance of S-vacancy on its surface. S vacancies provided more active sites and contact sites, which were favorable for the transfer of electrons, and the enhancement of its catalytic activity.

N_2 adsorption–desorption isotherms were adopted to analyze SSAs and pore size distributions (PSDs) of the $NiCo_2S_4$@N,S-rGO, $NiCo_2S_4$, and N,S-rGO. As illustrated in Fig. 4a, all isotherms exhibited typical IV curves of hysteresis loop at the higher relative pressure (0.45–1.0), demonstrating their mesoporous structure. The SSA of $NiCo_2S_4$@N,S-rGO was calculated to be 155.8 $m^2\ g^{-1}$, which was ~2-fold greater than that of $NiCo_2S_4$ (54.2 $m^2\ g^{-1}$). The dominant PSDs of ~7–9 nm for three mesoporous materials are shown in Fig. 4b. Collectively, the enlarged SSAs and the mesoporous characteristics provide a large number of active sites and more charge transfer channels, which are beneficial to adsorption and catalytic reaction, and thus improve the enzyme–mimetic activity of $NiCo_2S_4$@N,S-rGO.

3.2 Peroxidase-like and oxidase-like activities of the $NiCo_2S_4$@N,S-rGO nanocomposite

To verify the feasibility of the $NiCo_2S_4$@N,S-rGO sensor, we detected the UV-vis absorption of eight reaction systems at 652 nm (Fig. 5). In the presence of only TMB (system 1#), no 652 nm adsorption peak was observed. Similarly, the solution appeared colorless when containing only H_2O_2 (system 2#). In

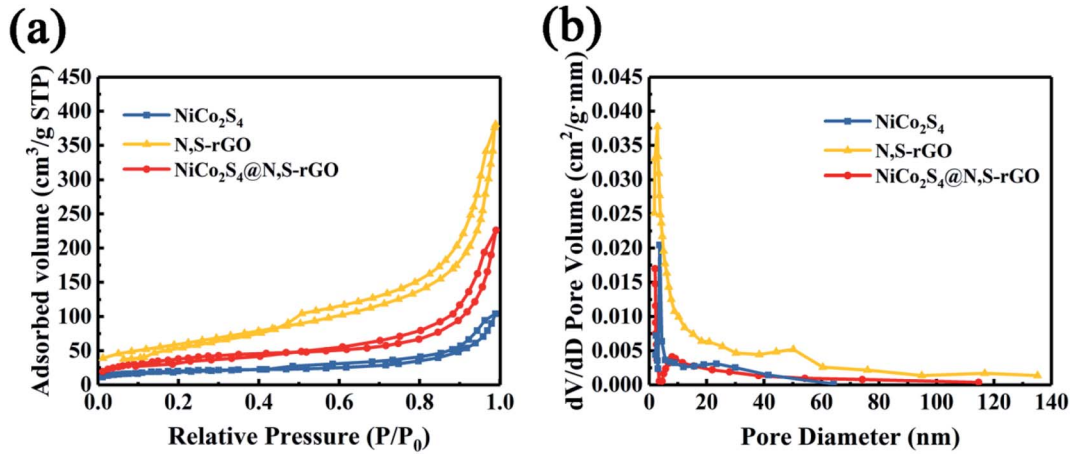

Fig. 4 (a) N_2 adsorption–desorption isotherms of $NiCo_2S_4$@N,S-rGO, $NiCo_2S_4$, and N,S-rGO; (b) The pore-size distribution of $NiCo_2S_4$@N,S-rGO, $NiCo_2S_4$, and N,S-rGO.

the simultaneous presence of H_2O_2 and TMB, the system 3# presented faint blue, illustrating that H_2O_2 could oxidize TMB to TMB_{Ox} in such a case. When the N,S-rGO (system 4#), $NiCo_2S_4$ (system 5#), or $NiCo_2S_4$@N,S-rGO (system 6#) were added to the TMB + H_2O_2 system, the solutions all exhibited the different degrees of blue color. Although the system 4# displayed light blue color, it was deeper than system 3#, probably because the doping of N and S led to more active sites in graphene and promoted the oxidation of TMB.[39] In stark contrast, the addition of $NiCo_2S_4$ (system 5#) yielded dark blue color, demonstrating

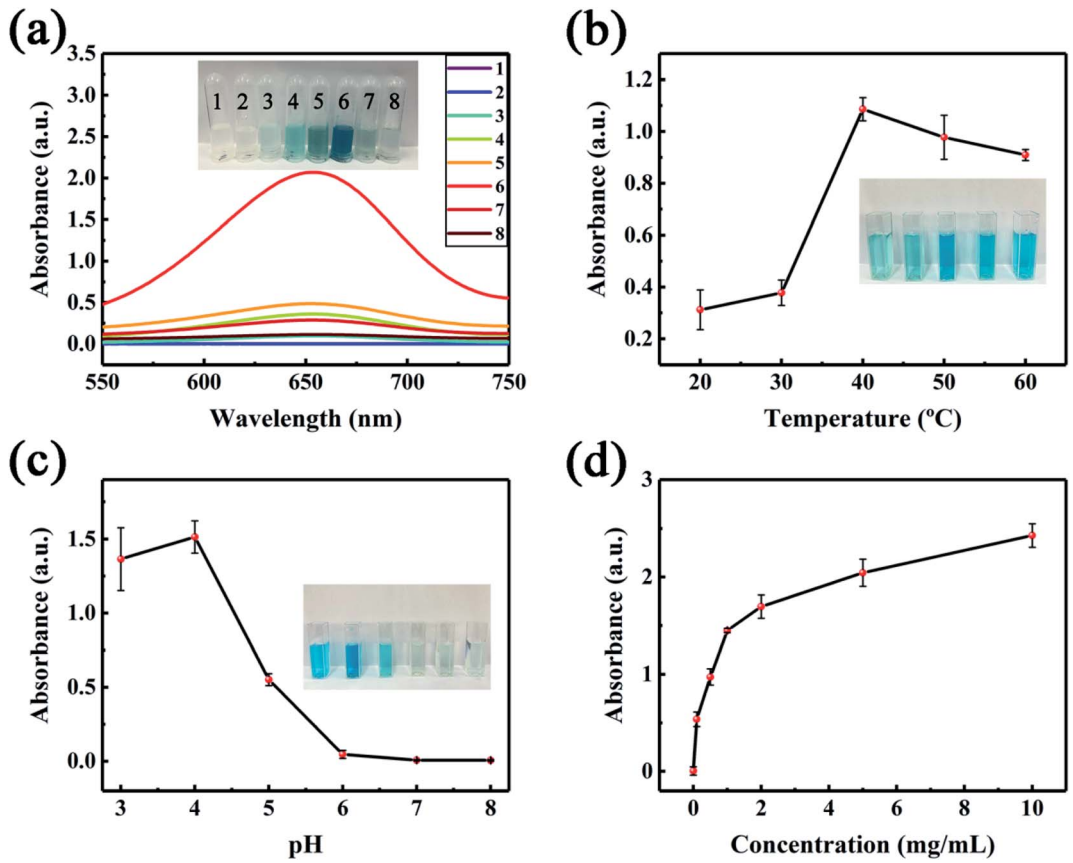

Fig. 5 (a) UV-vis absorption of the different reaction systems: 1, TMB; 2, H_2O_2; 3, TMB + H_2O_2; 4, r-GO + TMB + H_2O_2; 5, $NiCo_2S_4$+TMB + H_2O_2; 6, $NiCo_2S_4$@N,S-rGO + TMB + H_2O_2; 7, $NiCo_2S_4$@N,S-rGO + TMB; 8, $NiCo_2S_4$+TMB. Inset is photographs of the different reaction systems. Optimization of $NiCo_2S_4$@N,S-rGO peroxidase-like colorimetric system. (b) Absorbance of the system at different reaction temperatures (20–60 °C). (c) Absorbance of the system reaction at varying solution pH (3.0–8.0). (d) Absorbance of the reaction system with different concentrations of $NiCo_2S_4$@N,S-rGO (0–40 mg L^{-1}). Inset is the photographs in different reaction systems.

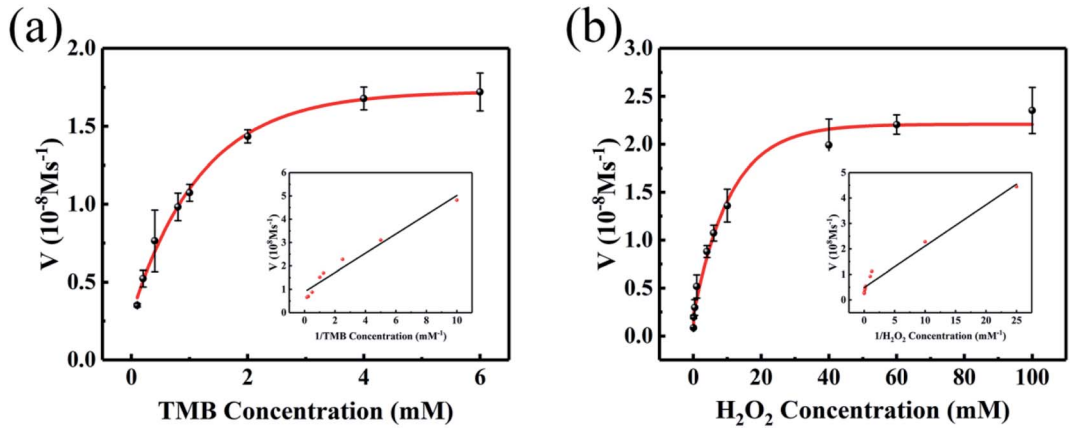

Fig. 6 Steady-state kinetic assay of the $NiCo_2S_4$@N,S-rGO. Michaelis–Menten curves for the $NiCo_2S_4$@N,S-rGO nanozyme: (a) the concentration of TMB is in the range of 0.1–6.0 mM; (b) the concentration of H_2O_2 is in the range of 0.04–100 mM. Insets are the double reciprocal plots of Michaelis–Menten equation against the concentrations of TMB or H_2O_2.

that $NiCo_2S_4$ could promote the oxidation of TMB. The system 6# produced the deepest blue color due to the co-presence of TMB, H_2O_2, and $NiCo_2S_4$@N,S-rGO, reflecting in the most intense characteristic peak at 652 nm. These findings illustrate that the $NiCo_2S_4$@N,S-rGO nanocomposite has a superior ability to oxidize TMB to TMBox, resulting from its larger SSA and rich vacant sites. Worth noting, the systems 7# (TMB + $NiCo_2S_4$@N,S-rGO) and 8# (TMB + $NiCo_2S_4$) displayed the different degrees of blue, evidencing that both the $NiCo_2S_4$ and $NiCo_2S_4$@N,S-rGO also possessed the oxidase-like activity.

3.3 Optimization of the system 6# (TMB + H_2O_2+$NiCo_2S_4$@N,S-rGO)

To achieve the best catalytic efficiency, we optimized the important parameters in the system 6#, including incubation temperature, solution pH, and nanocomposite concentration. As depicted in Fig. 5b, the 652 nm absorbance increased with increases in temperature from 20 to 40 °C; however, the further rising temperature (40–60 °C) led to decreased absorbance intensity. Too low temperature was not conducive to the catalytic oxidation of TMB by $NiCo_2S_4$@N,S-rGO, but too high temperature will lead to the inactivation of TMB. As a result, the deepest blue in the system 6# appeared at 40 °C (inset of Fig. 5a). Under basic conditions, H_2O_2 could be decomposed into O_2 and H_2O, thereby greatly abating the catalytic activity. Under strong acidic conditions, the electron-cloud density of N atoms in TMB was reduced, thus weakening the intermolecular interactions between $NiCo_2S_4$@N,S-rGO and substrate. Consequently, too high or low solution pH was both unfavorable for the oxidation reaction of TMB. It is obvious in Fig. 5c that the 652 nm absorbance was sharply reduced from pH 4.0 to 6.0, and almost no absorbance occurred from pH 6.0 to 8.0. Thus, we posit that the appropriate solution pH was 4.0. Over the concentration range of 0–10 mg mL^{-1}, the addition of nanocomposite caused the gradual increase in the 652 nm absorbance (Fig. 5d). Especially, when the fortified concentration varied from 0 to 1.0 mg mL^{-1} (0, 0.1, 0.5, and 1.0 mg mL^{-1}), the 652 nm optical densities (ODs) were dramatically enhanced, while slightly increased at 1.0–10.0 mg mL^{-1}. In the UV-vis detection systems, excessive ODs (>2.0) lead to a sharp decline in the responsivity of color recognition due to saturated absorbance. Based on the above findings, 1.0 mg mL^{-1} of the $NiCo_2S_4$@N,S-rGO nanocomposite was considered as the appropriate spiking level in the subsequent trials.

Table 1 Comparison of the Michaelis–Menten constants (K_m and V_{max}) for $NiCo_2S_4$@N,S-rGO catalyzed oxidation of H_2O_2

Catalyst	Substrate	K_m(mM)	V_{max}(10^{-8} M s^{-1})	Ref.
N,S-rGO	H_2O_2	3.8918	0.2672	This work
	TMB	0.6887	0.3706	
$NiCo_2S_4$	H_2O_2	0.4686	1.0815	This work
	TMB	0.4628	1.1212	
$NiCo_2S_4$@N,S-rGO	H_2O_2	0.3326	2.0479	This work
	TMB	0.3372	1.4956	
HRP	H_2O_2	3.7	8.71	41
	TMB	0.434	10	
Cu–Ag/rGO	H_2O_2	0.634	4.2553	42
	TMB	8.6145	7.0175	
WS_2/rGO	H_2O_2	10.001	0.9332	43
	TMB	22.406	0.9606	

Table 2 Comparison of the analytical performance of $NiCo_2S_4$@N,S-rGO based colorimetric assay with other colorimetric assay of glucose[a]

Nanomaterials	LRs (μM)	LODs (μM)	Ref.
CoOOH nanoflakes	5.3–500	1.20	51
r-CDs	10–400	2.00	52
$CoSe_2$/rGO	5–800	0.55	53
$NiCo_2O_4$	2–100	1.62	54
$NiCo_2S_4$@N,S-rGO	1–200	0.30	This work

[a] LRs and LODs denote the abbreviations of linear ranges and limits of detection, respectively.

3.4 Steady-state kinetics of the $NiCo_2S_4$@N,S-rGO

A typical Michaelis–Menten equation was used to investigate the steady-state kinetics of this colorimetric sensor based on the as-fabricated nanocomposite. TMB and H_2O_2 were chosen as substrates, and each experiment was performed in triplicate by varying the concentration of one substrate (Fig. 6). As well known, a lower K_m value denote a higher affinity between nanozyme and substrate.[40] As listed in Table 1, the K_m values offered by the nanocomposite were in the range of 0.3326–0.3372 at varying TMB and H_2O_2 levels. Consequently, the affinity by the nanocomposite increased by ~40% and 1.1~10.6-fold as compared to $NiCo_2S_4$ and N,S-rGO, respectively. Also, the $NiCo_2S_4$@N,S-rGO provided higher affinity than the common HRP,[41] as well as previously reported Cu–Ag/rGO[42] and WS_2/rGO.[43] These data evidence that the $NiCo_2S_4$@N,S-rGO greatly enhances the peroxidase-like activity.

3.5 Catalytic mechanism of this nanocomposite

Up to now, many kinds of mechanisms have been proposed to illustrate the catalytic oxidation of TMB by nanozyme, which are mainly involved in several species of reactive oxygen species (ROS), such as $^{\bullet}OH$, $^{\bullet}O_2^-$, and h^+.[44,45] Herein, we employed three ROS trappers (IPA, PBQ, and EDTA) to scavenge $^{\bullet}OH$, $^{\bullet}O_2^-$, and h^+, respectively. In contrast to the control group (no scavenger), the system color only slightly decreased after the addition of IPA, while more obvious fading phenomenon occurred upon the addition of both PBQ and EDTA (Fig. 7a). Especially, the system color became almost colorless following the addition of EDTA. These observations suggest that the mechanism regarding the nanocomposite-catalyzed oxidation of TMB is likely due to the common participation of three ROS species in the system. 5,5-Dimethyl-1-pyrroline N-oxide (DMPO) is able to trap ROS transiently, forming DMPO/radical spin adducts capable of forming signals of different shapes. Fig. 7b displays the standard quadruplet with the signal of 1 : 2 : 2 : 1, which is the plot of DMPO/$^{\bullet}OH$. Clearly, the high noise and weak signal intensity indicated that only a small amount of $^{\bullet}OH$ was generated in this system. As vividly elaborated in Fig. 7c, the plot of DMPO/$^{\bullet}O_2^-$ illustrated the production of $^{\bullet}O_2^-$ in the system. When compared to the plot of DMPO/$^{\bullet}OH$, the lower noise and higher signal intensity demonstrated that the amount of $^{\bullet}O_2^-$ was higher than that of $^{\bullet}OH$. The profile of photo-generated holes (h^+) is shown in Fig. 7d, and the strong signal provided compelling evidence that h^+ was the main active species in the nanocomposite-based enzyme catalytic system. These ESR observations were highly consistent with those of ROS scavengers, and thus the catalytic activity of $NiCo_2S_4$@N,S-

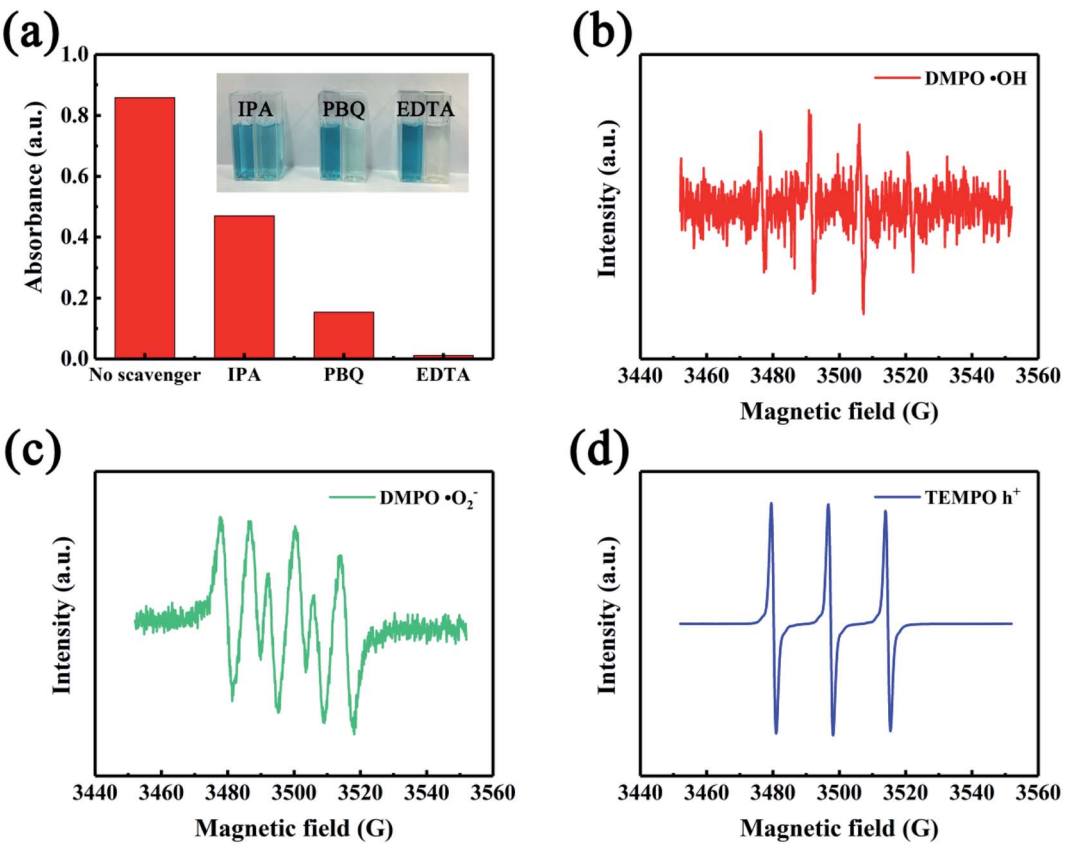

Fig. 7 Mechanistic study of $NiCo_2S_4$@N,S-rGO catalyzed oxidation of TMB. (a) Free radical scavenging experiment in the $NiCo_2S_4$@N,S-rGO reaction system. Insets are the photographs under different radical scavengers. (b) EPR spectra of $^{\bullet}OH$ in the $NiCo_2S_4$@N,S-rGO chromogenic system. (c) EPR spectra of $^{\bullet}O_2^-$ in the $NiCo_2S_4$@N,S-rGO chromogenic system. (d) EPR spectra of photogenerated holes (h^+) in the $NiCo_2S_4$@N,S-rGO chromogenic system.

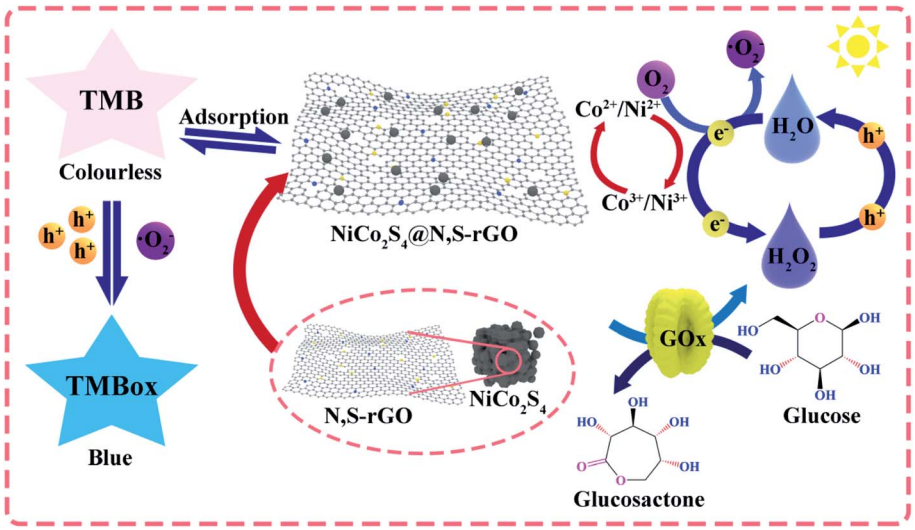

Scheme 1 Schematic representation of the $NiCo_2S_4$@N,S-rGO as a peroxidase mimetic for H_2O_2 and cholesterol detection.

rGO resulted from three radicals collectively and was dominated by h^+.

Building upon the above analyses, we speculate that the catalytic mechanisms of $NiCo_2S_4$@N,S-rGO are involved in three aspects: (1) As for this catalytic reaction, TMB molecules can be adsorbed onto the surface of nanocomposite through π–π interactions along with electrostatic attraction. The co-doping of N and S on rGO nanosheets provides abundant functional groups to facilitate the interactions with TMB, thereby improving the catalytic efficiency.[46] Meanwhile, the large SSA of $NiCo_2S_4$@N,S-rGO increased the active sites of its precursor $NiCo_2S_4$. (2) Under irradiation of visible light, the electrons of $NiCo_2S_4$ are excited at the conduction band (CB), holes are generated at the valence band (VB), and the transfer from CB to VB is promoted by N and S-doped rGO. With the participation of electrons (e^-), H_2O_2 is converted into O_2, which further forms $^{\bullet}O_2^-$. On the contrary, TMB loses e^- to form TMB_{Ox} in the reaction with $^{\bullet}O_2^-$ and/or h^+. (3) N and S co-doping, rich S-vacancy, and complex chemical valence states for the $NiCo_2S_4$@N,S-rGO facilitate electron transfer and accelerate the reaction progress.[47] The schematic illustration on the catalytic mechanisms of $NiCo_2S_4$@N,S-rGO is shown in Scheme 1. Wang's group concluded that catalyst interface structural engineering is advantageous in promoting electronic interactions, bringing redistribution of charges in heterogeneous catalysts, and creating an internal electric field.[48] This will further induce the formation of ion holes, which can play a bridging role in the reaction and transfer to the reactants, thus enhancing the catalytic activity. Furthermore, this effect is also influenced by the size effect of the nanomaterial on the interfacial support, *i.e.*, in small-sized nanomaterials, the effect is significantly enhanced by the large charge transfer per atom. Collectively, these findings obtained in this study are a good verification of the above-described theory; that is to say that the co-doping of hybrid atoms and the synergistic effect between $NiCo_2S_4$ and GO jointly promotes the catalysis of nanozyme.

3.6 H_2O_2 and glucose assay using the $NiCo_2S_4$@N,S-rGO based clorimetric reaction

Because the activity of $NiCo_2S_4$@N,S-rGO peroxidase was related to H_2O_2 concentration, the quantitative H_2O_2 assay could be achieved by measuring the 652 nm ODs. Fig. 8a–b displays the 652 nm absorbance *vs.* H_2O_2 concentration, which offers a good linear relationship from 0.04 to 50 mM with high correlation coefficient (R^2) of 0.9989 and low detection limit (LOD) of 12 μM. In three fortification levels (50, 500, and 1000 μM), the relative recoveries were in the range of 98.9–102.4% with relative standard deviations (RSDs) of 2.6–4.5%, demonstrating a high experimental accuracy (Table 3).

Additionally, glucose can be oxidized by GOx to produce H_2O_2, which is closely related to the peroxidase activity of natural enzyme or nanozyme. As a result, traditional HRP could be are replaced by $NiCo_2S_4$@N,S-rGO for glucose colorimetric assay. As the concentration of glucose increased, the amount of H_2O_2 increased in concomitant with the rising 652 nm ODs and enhancement of blue color under the catalysis of nanocomposite (Fig. 8a and b). Under optimized conditions (solution pH 4.0, 1.0 mg mL^{-1} nanocomposite, 20 min incubation at 40 °C), a plot of the 625 nm ODs against glucose concentrations was constructed with the linear equation of $y = 0.00141x + 0.1176$, as well as the correlation coefficient of 0.9788 (Fig. 8a). The linear range (LR) for glucose assay was 1.0–200 μM, and the limit of quantification (LOQ) and limit of detection (LOD) were 1.0 and 0.3 μM, respectively, based the 3-fold and 10-fold signal to noise (S/N = 3 and 10).[49,50] These analytical performance metrics were compared to several glucose assays by employing sensors based on other nanomaterials (Table 2). Evidently, this $NiCo_2S_4$@N,S-rGO nanoenzymatic biosensor achieves a much lower LOD (0.30 μM) than those of CoOOH nanoflakes (1.20 μM),[51] r-CDs (2.00 μM),[52] $CoSe_2$/rGO (0.55 μM),[53] and $NiCo_2O_4$ (1.62 μM).[54] Also, it offers a relatively wider LR (1.0–200 μM) in contrast to other approaches. As such, these comparative

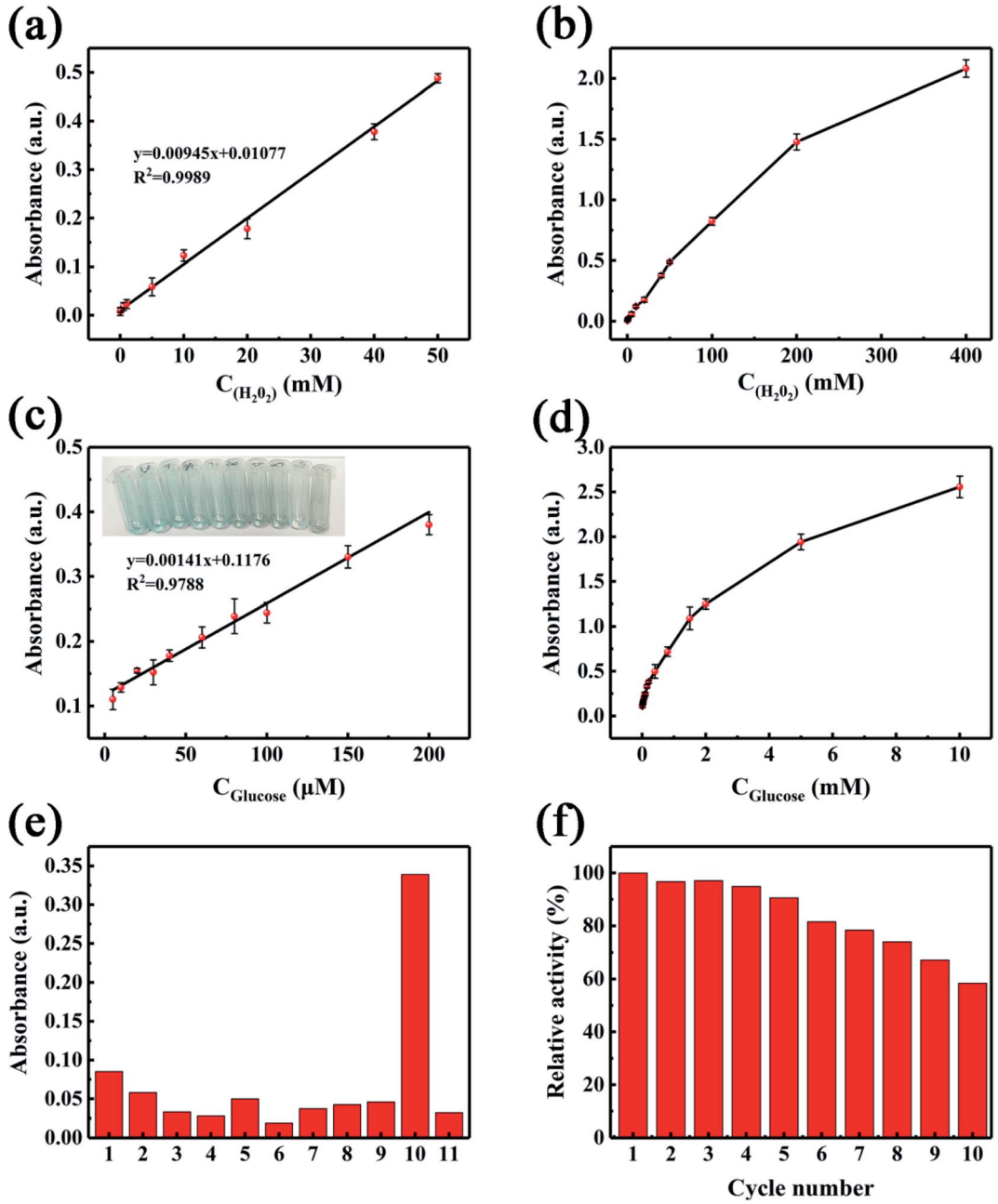

Fig. 8 (a) Calibration curve of absorbance *vs.* H_2O_2. (b) Real response curve of absorbance *vs.* H_2O_2 concentration. (c) Calibration curve of absorbance *vs.* glucose. (d) Real response curve of absorbance *vs.* glucose concentration. (e) Selectivity of this nanozymic sensing method for glucose. 1, Histidine; 2, Sucrose; 3, Galactose; 4, Fructose; 5, Serine; 6, Ascorbic acid; 7, K^+; 8, Mg^{2+}; 9, Na^+; 10, Glucose; and 11, Blank. With the exception of glucose, each interference macromolecule or ion was fortified at 5.0 μg mL^{-1}. (f) Reproducibility results of this nanozyme sensing method.

performance metrics demonstrate that the as-constructed nanozymic biosensor is conducive to practical applications in the analytical field of biomolecules.

3.7 Selectivity/anti-interference effect and reusability of the nanocomposite-based colorimetric method for glucose assay

A series of anti-interference experiments were conducted to assess the selectivity of this proposed method under optimized conditions. The co-existing components in human serum

Table 3 The fortified recovery for H_2O_2 based on the colorimetric assay of $NiCo_2S_4$@N,S-rGO[a]

Samples	Added (μM)	Found (μM)	Recovery (%)	RSDs (%, n = 6)
Human serum	—	—	—	—
	50	51.2	102.4	2.6
	500	494.4	98.9	4.5
	1000	992.6	99.3	4.3

[a] RSDs represent relative standard deviations.

Table 4 Reliability of this colorimetric assay for glucose based on $NiCo_2S_4$@N,S-rGO

Samples	Determined by a glucometer (mM)	Determined by this method (mM)	Added (μM)	Found (μM)	Recovery (%)	RSDs (%, $n = 6$)
Serum 1#	15.62	16.13	5	4.87	97.4	3.12
Serum 2#	5.29	5.42	5	5.09	101.8	2.14

samples include fructose, galactose, sucrose, serine, histidine, ascorbate, K^+, Ca^{2+}, Na^+, and so on. These components were added at 5.0 μg mL^{-1} to the diluted serum samples, as described in Section 2.5. As detailed in Fig. 8e, the interference macromolecules/ions had less influences on the 625 nm ODs. It was worth noting that when compared to the blank sample, the 625 nm absorbance reduced to a certain degree following the addition of ascrobic acid, reflecting in the fading of blue color. This phenomenon may be explained by that owing to the reductive property of ascorbic acid, it consumed H_2O_2, one of the main products in the GOx-catalyzed reaction. The reusability of $NiCo_2S_4$@N,S-rGO as nanozyme is displayed in Fig. 8f. The relative activity remained as high as 81.9% after reusing 6 times, while 58.6% after 10 times. Thus, we posit that the as-fabricated nanozyme can be repeatedly used as a colorimetric sensor at least 6 times.

The feasibility of the as-constructed sensor was evaluated by detecting glucose contents in human serum samples. The concentrations of glucose in two serum samples were detected to be 15.62 and 5.29 μM, while they were 16.12 and 5.42 μM, respectively, by a blood glucose meter. Consequently, the acquired relative recoveries spanned the range of 97.4–101.8% with RSDs of 2.14–3.12% (Table 4). These data/findings offer strong evidence that this colorimetric method based on the $NiCo_2S_4$@N,S-rGO nanozyme can provide a satisfactory experimental accuracy/precision for glucose assay in human serum samples.

4 Conclusions

Herein, we fabricated the nanocomposite ($NiCo_2S_4$@N,S-rGO) by a facile calcining approach, and its structure was characterized in detail by virtue of a series of spectral techniques, such as XRD, HRTEM, SEM, and FT-IR. The $NiCo_2S_4$@N,S-rGO possessed significantly higher peroxidase-like activity than its precursors ($NiCo_2S_4$ and N,S-rGO), which resulted from the N, S-codoping, rich S-vacancy, and multi-valence states of this nanocomposite. This nanomaterial had typical mesopore structure (pore size of ~7–9 nm), and its SSA increased by ~2-fold over that of $NiCo_2S_4$, thus producing more active sites and charge transfer channels. Based on ROS scavenging experiments, the enhanced peroxidase–mimetic activity is confirmed to be the combined action of ROS ($^{\bullet}OH$, $^{\bullet}O_2^-$, and h^+), among which h^+ was dominated in the TMB-based chromogenic reaction. Under optimized conditions, the nanocomposite-based sensor gave lower LODs of 12 μM for H_2O_2 and 0.3 μM for glucose, respectively and comparable detection results in contrast to traditional glucose meter. Overall, this work provides a feasible strategy for developing bimetallic sulfides for H_2O_2 and glucose detection in complex human fluid samples.

Conflicts of interest

The authors declare no conflict of interest.

Acknowledgements

This work was jointly supported by the National Science Foundation of China (22076134 and 21876125), Jiangsu Provincial Natural Science Foundation (BK20211338) and Key Research & Development program (BE2022733), as well as Key Science & Technology Project of Suzhou City (SS202028).

Notes and references

1 J. B. Cole and J. C. Florez, *Nat. Rev. Nephrol.*, 2020, **16**, 377–390.
2 R. K. Mahat, N. Singh, M. Arora and V. Rathore, *Diabetes, Metab. Syndr.*, 2019, **13**, 2803–2811.
3 M. H. U. Rehman, A. Ahmad, R. M. Amir, K. Ameer, S. W. Ali, F. Siddique, I. Hayat, Z. Ahmad and F. Faiz, *Food Sci. Technol.*, 2021, **41**, 349–354.
4 H. Y. Chen, A. J. Fang, L. He, Y. Y. Zhang and S. Z. Yao, *Talanta*, 2017, **164**, 580–587.
5 M. B. Hall and N. S. Keuler, *J. AOAC Int.*, 2009, **92**, 50–60.
6 L. A. Zhang, C. C. Gu, H. Ma, L. L. Zhu, J. J. Wen, H. X. Xu, H. Y. Liu and L. H. Li, *Anal. Bioanal. Chem.*, 2019, **411**, 21–36.
7 M. R. Zhang, Y. X. Liu, J. X. Wang and J. G. Tang, *Microchim. Acta*, 2019, **186**, 83.
8 X. Chen, H. Wan, R. Guo, X. Wang, Y. Wang, C. Jiao, K. Sun and L. Hu, *Microsyst. Nanoeng.*, 2022, **8**, 48.
9 S. Yin, J. Wang, Y. Li, T. Wu, L. Song, Y. Zhu, Y. Chen, K. Cheng, J. Zhang, X. Ma, L. Donghai and G. Chen, *Electroanalysis*, 2021, **33**, 2216–2225.
10 A. Othmani, A. Maddouri, M. Derbali, F. Touati and H. Dhaouadi, *J. Mater. Sci.: Mater. Electron.*, 2022, **33**, 7048–7057.
11 K. C. Lu, J. K. Wang, D. H. Lin, X. Chen, S. Y. Yin and G. S. Chen, *Anal. Methods*, 2020, **12**, 2661–2667.
12 M. Filip, M. Vlassa, V. Coman and A. Halmagyi, *Food Chem.*, 2016, **199**, 653–659.
13 J. D. Oliver, A. A. Rosser, C. M. Fellows, Y. Guillaneuf, J.-L. Clement, M. Gaborieau and P. Castignolles, *Anal. Chim. Acta*, 2014, **809**, 183–193.
14 M. Pleitez, H. von Lilienfeld-Toal and W. Mantele, *Spectrochim. Acta, A*, 2012, **85**, 61–65.

15 Y. F. Chen, Y. Zhang, L. Jiao, H. Y. Yan, W. L. Gu and C. Z. Zhu, *Chin. J. Anal. Chem.*, 2021, **49**, 907–921.
16 Q. W. Liu, A. Zhang, R. H. Wang, Q. Zhang and D. X. Cui, *Nano-Micro Lett.*, 2021, **13**, 154.
17 M. Wei, J. Lee, F. Xia, P. H. Lin, X. Hu, F. Y. Li and D. S. Ling, *Acta Biomater.*, 2021, **126**, 15–30.
18 B. Peng, J. M. Xu, M. M. Fan, Y. Guo, Y. J. Ma, M. Zhou and Y. J. Fang, *Anal. Bioanal. Chem.*, 2020, **412**, 861–870.
19 F. Honarasa, F. H. Kamshoori, S. Fathi and Z. Motamedifar, *Microchim. Acta*, 2019, **186**, 234.
20 L. Gao, J. Zhuang, L. Nie, J. Zhang, Y. Zhang, N. Gu, T. Wang, J. Feng, D. Yang, S. Perrett and X. Yan, *Nat. Nanotechnol.*, 2007, **2**, 577–583.
21 Q. Liu, P. Tang, X. Xing, W. Cheng, S. Liu, X. Lu and L. Zhong, *Talanta*, 2022, **240**, 123118.
22 P. K. Yadav, V. K. Singh, S. Chandra, D. Bano, V. Kumar, M. Talat and S. H. Hasan, *ACS Biomater. Eng.*, 2019, **5**, 623–632.
23 J. Y. Chen, Y. Shu, H. L. Li, Q. Xu and X. Y. Hu, *Talanta*, 2018, **189**, 254–261.
24 S. F. Cai, Q. S. Han, C. Qi, Z. Lian, X. H. Jia, R. Yang and C. Wang, *Nanoscale*, 2016, **8**, 3685–3693.
25 X. Zhou, M. Wang, J. Chen and X. Su, *Talanta*, 2022, **245**, 123451.
26 X. L. Liu, X. H. Wang, Q. S. Han, C. Qi, C. Wang and R. Yang, *Talanta*, 2019, **203**, 227–234.
27 Y. L. He, N. Li, X. W. Liu, W. Chen, X. X. Zhu and Q. Y. Liu, *Microchim. Acta*, 2021, **188**, 172.
28 Q. Zhao, X. Y. Zheng, L. Xing, Y. L. Tang, X. M. Zhou, L. Hu, W. L. Yao and Z. Q. Yan, *J. Hazard. Mater.*, 2021, **409**, 125019.
29 S. W. Lv, N. Zhao, J. M. Liu, F. E. Yang, C. Y. Li and S. Wang, *ACS Appl. Mater. Interfaces*, 2021, **13**, 25044–25052.
30 K. L. Wu, B. C. Yang, X. X. Zhu, W. Chen, X. L. Luo, Z. X. Liu, X. Zhang and Q. Y. Liu, *New J. Chem.*, 2018, **42**, 18749–18758.
31 P. Borthakur, P. K. Boruah and M. R. Das, *ACS Sustainable Chem. Eng.*, 2021, **9**, 13245–13255.
32 L. S. Wei, Q. S. Wu and J. F. Li, *J. Mater. Sci.*, 2021, **32**, 12966–12990.
33 J. Li, Q. F. Wang, K. Liu, J. B. Jiang, D. Qian, J. H. Li and Z. H. Chen, *Mater. Lett.*, 2017, **186**, 189–192.
34 N. H. Fu, X. Liang, Z. Li, W. X. Chen, Y. Wang, L. R. Zheng, Q. H. Zhang, C. Chen, D. S. Wang, Q. Peng, L. Gu and Y. D. Li, *Nano Res.*, 2020, **13**, 947–951.
35 W. Liu, J. Zhou, D. Liu, S. Liu and X. Liu, *Mater. Lett.*, 2022, **307**, 131076.
36 S. M. Mane, S. S. Pawar, J. Seong Go, A. M. Teli and J. Cheol Shin, *Mater. Lett.*, 2021, **301**, 130262.
37 Y. Zhu, J. Li, X. Yun, G. Zhao, P. Ge, G. Zou, Y. Liu, H. Hou and X. Ji, *Nano-Micro Lett.*, 2020, **12**, 16.
38 A. C. Ferrari and D. M. Basko, *Nat. Nanotechnol.*, 2013, **8**, 235–246.
39 C. Liu, L. Q. Zhang, R. Liu, Z. F. Gao, X. P. Yang, Z. Q. Tu, F. Yang, Z. Z. Ye, L. S. Cui, C. M. Xu and Y. F. Li, *J. Alloys Compd.*, 2016, **656**, 24–32.
40 Y. L. Dong, H. G. Zhang, Z. U. Rahman, L. Su, X. J. Chen, J. Hu and X. G. Chen, *Nanoscale*, 2012, **4**, 3969–3976.
41 N. Lu, M. Zhang, L. Ding, J. Zheng, C. Zeng, Y. Wen, G. Liu, A. Aldalbahi, J. Shi, S. Song, X. Zuo and L. Wang, *Nanoscale*, 2017, **9**, 4508–4515.
42 G. Darabdhara, B. Sharma, M. R. Das, R. Boukherroub and S. Szunerits, *Sens. Actuators, B*, 2017, **238**, 842–851.
43 S. Keerthana, A. Rajapriya, C. Viswanathan and N. Ponpandian, *J. Alloys Compd.*, 2021, **889**, 161669.
44 Y. X. Zhuang, X. D. Zhang, Q. M. Chen, S. Q. Li, H. Y. Cao and Y. M. Huang, *Mater. Sci. Eng.*, 2019, **94**, 858–866.
45 J. K. Fu, Y. R. Shao, L. Y. Wang and Y. C. Zhu, *Nanoscale*, 2015, **7**, 7275–7283.
46 P. Das, P. Borthakur, P. K. Boruah and M. R. Das, *J. Chem. Eng. Data*, 2019, **64**, 4977–4990.
47 B. H. Zhang, H. X. Wang, Z. Zuo, H. S. Wang and J. T. Zhang, *J. Mater. Chem. A*, 2018, **6**, 15728–15737.
48 H. Wang, K. Y. Xie, Y. You, Q. Hou, K. Zhang, N. Li, W. Yu, K. P. Loh, C. Shen and B. Q. Wei, *Adv. Energy Mater.*, 2019, **9**, 1901806.
49 A. K. Rivas-Sanchez, D. S. Guzman-Hernandez, M. T. Ramirez-Silva, M. Romero-Romo and M. Palomar-Pardave, *Dyes Pigm.*, 2021, **184**, 108641.
50 M. Safdarian, P. Hashemi and A. Ghiasvand, *Food Chem.*, 2021, **343**, 128481.
51 Y. M. Wang, J. W. Liu, J. H. Jiang and W. Zhong, *Anal. Bioanal. Chem.*, 2017, **409**, 4225–4232.
52 Y. J. Long, X. L. Wang, D. J. Shen and H. Z. Zheng, *Talanta*, 2016, **159**, 122–126.
53 X. Tian, X. Wang, C. Dai, Y. Li, C. Yang, Z. Zhou and Y. Wang, *Sens. Actuators, B*, 2017, **245**, 221–229.
54 L. Su, W. Dong, C. Wu, Y. Gong, Y. Zhang, L. Li, G. Mao and S. Feng, *Anal. Chim. Acta*, 2017, **951**, 124–132.